Correlation between surface reconstruction and polytypism in InAs nanowire selective area epitaxy

Ziyang Liu,[1,2,*] Clement Merckling,[1] Rita Rooyackers,[1] Olivier Richard,[1] Hugo Bender,[1] Yves Mols,[1] María Vila,[3,4]
Juan Rubio-Zuazo,[3,4] Germán R. Castro,[3,4] Nadine Collaert,[1] Aaron Thean,[1] Wilfried Vandervorst,[1,5] and Marc Heyns[1,2]

[1]*imec, Kapeldreef 75, 3001 Leuven, Belgium*
[2]*Department of Materials Engineering, KULeuven, 3001 Leuven, Belgium*
[3]*SpLine CRG BM25 Beamline, European Synchrotron Radiation Facility, 71 Avenue des Martys, 38000 Grenoble, France*
[4]*Instituto de Ciencia de Materiales de Madrid, Consejo Superior de Investigaciones Científicas (ICMM -CSIC), 28049 Madrid, Spain*
[5]*Department of Physics and Astronomy, KULeuven, 3001 Leuven, Belgium*

The mechanism of widely observed intermixing of wurtzite and zinc-blende crystal structures in InAs nanowire (NW) grown by selective area epitaxy (SAE) is studied. We demonstrate that the crystal structure in InAs NW grown by SAE can be controlled using basic growth parameters, and wurtzitelike InAs NWs are achieved. We link the polytypic InAs NWs SAE to the reconstruction of the growth front (111)B surface. Surface reconstruction study of InAs (111) substrate and the following homoepitaxy experiment suggest that (111) planar defect nucleation is related to the (1×1) reconstruction of InAs (111)B surface. In order to reveal it more clearly, a model is presented to correlate growth temperature and arsenic partial pressure with InAs NW crystal structure. This model considers the transition between (1×1) and (2×2) surface reconstructions in the frame of adatom atoms adsorption/desorption, and the polytypism is thus linked to reconstruction quantitatively. The experimental data fit well with the model, which highly suggests that surface reconstruction plays an important role in the polytypism phenomenon in InAs NWs SAE.

I. INTRODUCTION

III–V nanowires (NWs) on silicon are important building blocks for future electrical and optical devices [1,2]. Basically, they can be fabricated either by a vapor-liquid-solid (VLS) [3–8] or a noncatalytic approach, in which selective area epitaxy (SAE) is especially an attractive method for its compatibility to the complementary metal-oxide semiconductor (CMOS) process [9,10]. Irrespective of the growth method, wurtzite (WZ)/zinc-blende (ZB) polytypism phenomenon caused by (111) planar defects (PDs) are widely observed [11–25], which could cause a key challenge for applications [26–29] but also make interesting polytypic structures possible [30,31].

Polytypism is a fundamental topic in crystal growth [32,33], and NWs epitaxy provides an ideal study system, since other types of threading defects are normally absent. Great progress has been made in crystalline phase control in NW VLS growth. For a wide range of III–V NWs, the crystal structure can be engineered from ZB to WZ using the parameters like temperature, V/III ratio, growth rate, doping, and NW diameter [5,12,17–20,22,34–42]. It is generally related to the affinity between the ZB and WZ phase in critical energy during nucleation in the $(\overline{1}\overline{1}\overline{1})$ or $(000\overline{1})$ basal plane, which is the growth front for most III–V NWs [43,44]. A classic nucleation model is widely adopted to explain the experimental observation [14,45].

In contrast, most III–V NWs grown by SAE are still troubled by a high density of randomly distributed PDs [46]. The only exception is the pure WZ phase InP NW, which can be achieved by growing in (111)A orientation instead of normally used (111)B and growth parameter tuning [28,47]. Some work has been performed on Ga(In)As NWs by studying the

impact of growth temperature but a pure crystal phase (either ZB or WZ) has not been demonstrated [48–51]. Although SAE provides a different perspective of this phenomenon with no liquid phase involved [52–54], the understanding of the details of the mechanism is still far from complete [47,48,50,51,55,56]. Although surface reconstruction has been suspected as a key factor that drives the polytypism in GaAs NW SAE in some studies [47,48,51], it largely remains a hypothesis and there is even less report about polytypism in InAs NWs.

In this work, we study the control of polytypism in InAs NW SAE and reveal its relationship to the reconstruction of NW growth front (111)B surface. Facilitated by a method to quickly extract the percentage of WZ phase (hexagonality) in InAs NW using x-ray diffraction (XRD) [57], we systematically investigate the influence of growth parameters on the crystal structure of InAs NW in SAE. Wurtzitelike InAs NWs are achieved based on this study. The mechanism of PD formation and polytypism in NW SAE is studied, and the hypothesis that the surface reconstruction of InAs (111)B impacts the preference of crystal structure in nuclei is examined. An investigation of the surface reconstruction is performed on InAs (111)B substrate. The crystal structure of the homoepitaxial layer is surface reconstruction dependent. Moreover, the hexagonality in InAs NW can be linked to the growth conditions quantitatively by a model considering the surface reconstruction of the nuclei. The model is finally assessed by the experimental input.

II. EXPERIMENTAL DETAILS

InAs NWs were selectively grown on Si (111) substrate by a metal-organic vapor phase epitaxy (MOVPE) tool, using tertiarybutylarsine (TBAs) and trimethylindium (TMIn) as the arsenic and indium source respectively. The Si substrate was

---

*Corresponding author: ziyang.liu791@gmail.com

covered by a 20-nm-thick SiO_2 layer, in which holes with diameters ranging from 200 to 350 nm with different pitches are patterned before the InAs growth. A variety of growth parameters were used. A nucleation step was used to increase the vertical NW yield. Unless otherwise stated, the TMIn flow rate was kept at $1 \mu mol/min$. In order to guarantee a sufficient amount of InAs for characterization, growth time was varied to obtain an equivalent total TMIn flow injection of $60 \mu mol$ for different flow rates. More details of the growth can be found elsewhere [57]. Meanwhile, a surface reconstruction study was conducted on a 2-in. InAs (111)*B* substrate in a Riber molecular-beam epitaxy (MBE) system equipped with valved cracker cells of As. Reflective high-energy electron diffraction (RHEED) was performed to analyze the surface reconstruction. InAs (111)*B* substrate was first deoxidized at temperature of $630 °C$ under As_4 flux until a clear (1×1) reconstruction was observed in RHEED. Then the transition between (1×1) and (2×2) reconstructions was studied by varying the temperature and As_4 flux rate. The temperature was read and calibrated from a pyrometer.

InAs NWs were characterized by an FEI NOVA200 scanning electron microscope (SEM). To study the PD density, or hexagonality in the InAs NWs, high-resolution XRD (HR-XRD) was performed on a PANanlytical X'pert PRO diffractometer equipped with a Cu $K\alpha$ radiation source and a Ge (220) four-bounce monochromator. Transmission electron microscopy (TEM) was done on a Tecnai F30S TEM working under 300 kV. Images were taken along $\langle 110 \rangle$ zone axis in order to reveal the (111) PDs. Grazing-Incidence XRD (GIXRD) was performed on beamline BM25B, ESRF, with x-ray wavelength of 0.0826 nm [58]. InAs (111)*B* surface was investigated by a Bruker Edge atomic force microscope (AFM) under tapping mode.

III. CONTROL OF POLYTYPISM IN InAs NW SAE

The method to extract the PD frequency in SAE InAs NWs by XRD [57] facilitates systematic study of the impact of growth parameters (growth temperature, V/III ratio, growth rate, etc.) on polytypism. A series of experiments were conducted for this purpose, and the details of the growth parameters can be found in Table I. In the first set of experiments,

TABLE I. Details of growth parameters used in the studies of growth temperature, V/III ratio, and growth rate, respectively. A nucleation step was applied for each growth. Other growth parameters are the same.

	Temperature (°C)	TBAs flow ($\mu mol/min$)	TMIn flow ($\mu mol/min$)	V/III ratio
Growth temperature study	505 550 575 605	370	1	370
V/III ratio study	565	31 124 370	1	31 124 370
Growth rate study	550	185 370 1480	0.5 1 4	370

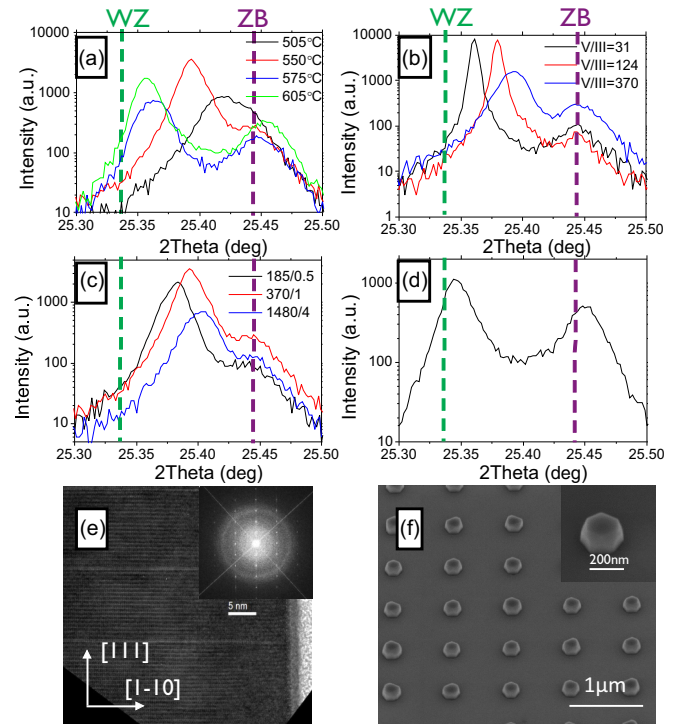FIG. 1. XRD 2θ-ω scan of InAs NWs grown under a variety of (a) temperatures, (b) V/III ratios, and (c) group-III flow rate ($\mu mol/min$). Details of the growth parameters are shown in Table I. (d) XRD 2θ-ω scan of InAs NW grown under growth condition that best favors WZ phase ($605 °C$, V/III = 31/0.5), The peak positions corresponding to ideal ZB and WZ InAs are represented by dashed lines. (e) The HRTEM picture of an InAs NW from the latter sample. The NW is largely in WZ phase with occasional stacking faults. The inset FFT pattern confirms hexagonal crystal structure. (f) Tilted view SEM image of the WZ phase InAs "NWs"; inset shows a single NW with top dome shape in higher resolution.

Samples were grown under different growth temperatures from 490 to $605 °C$, while the V/III ratio was 370 and other parameters were kept the same. HRXRD 2θ-ω scans were performed on these samples and are shown in Fig. 1(a). The reference Si (111) peaks are omitted to highlight the difference of InAs peaks, and the theoretic Bragg angle of ZB (111) and WZ (0002) InAs are indicated by a dashed line. There are two types of InAs peaks. The first one always stays at the ZB position irrespective of samples. It is related to the by-products (irregular blocks and coalesced islands) of InAs NW growth. In contrast, the other kind of peak locates at a variable position in between ZB and WZ diffraction position, which is the diffraction of the polytypic InAs NWs and termed as "mixed-phase peak." A detailed discussion about this double peak phenomenon can be found in Ref. [56]. The mixed-phase peak moves to a lower angle when a higher growth temperature is applied. This indicates that the InAs NWs become more hexagonal with increasing growth temperature. In the meantime, the effect of the V/III ratio is also studied in a similar manner. Here, the flow rate of TBAs was altered while the TMIn flow and other parameters were kept constant. The growth temperature was $565 °C$. HRXRD results are shown in Fig. 1(b). The InAs NW peak shifts to the lower angle values as the V/III ratio decreases.

Hence, higher hexagonality is obtained with lower V/III ratios. Besides, the influence of growth rate or TMIn flow rate is studied as well, where both the group-III and group-V flow rates were changed simultaneously while the V/III ratio was kept at 370. The growth temperature was 550 °C and other parameters were the same. Similar to the results shown previously, the InAs NW peak shifted to the hexagonal region for smaller total flow rate [Fig. 1(c)]. Interestingly, all these trends are similar to that reported in VLS growth [22]. However, in contrast to VLS growth, the NW diameter has little impact on hexagonality in SAE. For InAs NWs prepared under the same condition with diameters ranging from 30 to 350 nm, it is found that their hexagonalities are nearly the same by both HRTEM and XRD [24,57]. It should be attributed to the absence of liquid droplets and thus less impact of the Gibbs-Thompson effect [35,59].

Combining the previously mentioned factors, by using high growth temperature (605 °C), low V/III ratio, and small group III flow rate (i.e., III/V = 31/0.5), WZ-like InAs NWs were obtained. As shown in Fig. 1(d), the InAs NW mixed-phase peak is very close to the ideal WZ position, and the hexagonality is identified around 93% using our quantitative model [57]. The HRTEM picture in Fig. 1(e) and the corresponding fast Fourier transform (FFT) pattern shown in the inset confirms the NW is largely composed of a WZ structure with occasional stacking faults, which agrees well with the XRD results. The NWs are dome shaped [Fig. 1(f)], composed of $\{1\bar{1}00\}$, $\{10\bar{1}\bar{1}\}$, and $\{000\bar{1}\}$ facets. Interestingly, this morphology is similar to the widely studied wurtzite GaN NWs [2]. Due to the limited NW growth window, a compromise between crystal structure engineering and NW morphology needs to be reached. Further optimization is possible by adding more parameters (like doping and growth pressure) into the matrix or using pulse-mode growth techniques to further tune the morphology [60,61].

IV. InAs (111)*B* SURFACE: THE VARIABLE

NW growth follows a layer-by-layer manner by fast lateral expansion of single nucleus on growth front, unless the wire is very wide [62–64]. On the $\{111\}/\{0001\}$ basal plane, there are two possible stacking positions for the nuclei: ZB and WZ. For the III–V materials, the nucleation at the WZ site introduces additional energy due to the third-nearest-neighbor interaction (stacking fault energy). In this section, the reason a WZ segment would form in the ZB lattice is interpreted qualitatively in the classic nucleation model. Surface reconstruction is highlighted as an important factor that impacts the nucleation in NW SAE.

A. PD nucleation in NWs

The classic nucleation model [65,66] has been widely accepted to explain the polytypism phenomenon in NW, at least for VLS growth [13,14]. For a nucleus in circular shape with unit area per atom s_c, the critical energy of nucleation (barrier energy) is

$$\Delta G^* = \frac{\pi \gamma^2 s_c}{\Delta \mu - \Delta \sigma s_c}, \qquad (1)$$

where $\Delta \mu$ is the supersaturation, $\Delta \sigma$ is the interface energy, and γ is the edge energy.

The critical size, which corresponds to the energy barrier, is an important concept. Classic theory treats nuclei smaller than critical size as unstable clusters. In other words, the crystal structure of the nucleus is determined as it becomes stable at critical size. The preference over ZB or WZ nucleation is determined by their respective critical energies. In the case of ZB nucleation on ZB substrate, ideally, there is no interface energy. In contrast, for WZ nucleation on the ZB crystal, i.e., the PD formation, an extra stacking fault energy σ_F is introduced. Therefore, for ZB and WZ nucleation the energy barriers are as follows:

$$\Delta G^*_{ZB} = \frac{\pi \gamma^2_{ZB} s_c}{\Delta \mu}, \qquad (2)$$

$$\Delta G^*_{WZ} = \frac{\pi \gamma^2_{WZ} s_c}{\Delta \mu - \sigma_F s_c}, \qquad (3)$$

where γ_{ZB} and γ_{WZ} are the edge energy of ZB and WZ nuclei, respectively.

In the first impression, additional stacking fault energy makes the WZ phase less favorable during nucleation. It is the lower edge energy of WZ phase nuclei that compensates for the stacking fault energy penalty, and makes the crystal phase altering from ZB to WZ possible [13,14,59]. The crystal phase of each newly formed layer in NW is determined by that of the nucleus. The hexagonality of NW is thus related to the nucleation probability of WZ crystals [67].

More variables need to be considered in VLS growth based on this simplified model due to the involvement of the liquid droplet. It has been reported that the nucleation prefers to happen at the edge of the liquid (triple-phase line) due to the saved energy by replacing part of the liquid-vapor interface by a nucleus-vapor interface [14]. Hence, it brings more a complex equation containing the geometric information of liquid versus nucleus. Therefore, apart from supersaturation, the shape of the liquid droplet (size and contact angle) also plays a great role in the crystal phase of NWs [23,35,68,69]. It should also be noticed that a ZB substrate is assumed for the equations above. However, on the NW growth front, the crystal structure of the "substrate" is polytypic due to PD piling up in NWs and interface energy could change accordingly [70,71]. All studies until now have been limited to the qualitative or semiquantitative stage due to lacking knowledge about the edge energies and the difficulty in real-time measurement of the geometry between liquid and nuclei.

In SAE, the solid-vapor surface should be considered instead of the solid-liquid interface in VLS growth for nucleation. It is well known that the positions of atoms at the surface are varied from their bulk counterparts due to the relaxation (surface reconstruction) for energy minimization [72]. Therefore, the energies of the nuclei-vapor surface and the nuclei-substrate interface are in turn varied. The assumption of constant surface/interface energy is not true for SAE. The interface energy $\Delta \sigma'$ and surface energy difference between nucleus top and initial substrate surface $\Delta \gamma_{S(111)B}$ are both surface reconstruction dependent. This would introduce another significant variable in nucleation energy. The energy
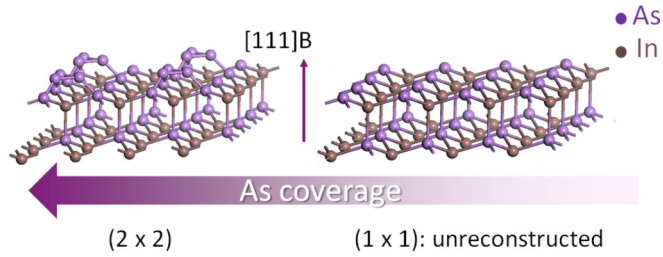
FIG. 2. Schematic atom and bond diagram of (2×2) and (1×1) surface reconstructions, where As and In atoms are represented by purple and brown spheres, respectively. (1×1) is nominally unreconstructed, while (2×2) has As trimers on top [81].

barrier for nucleation is then expressed as

$$\Delta G^* = \frac{\pi \gamma^2 s_c}{\Delta \mu - (\Delta \sigma' + \Delta \gamma_{s(111)B}) s_c}. \quad (4)$$

Obviously, the nucleation barrier is significantly influenced by surface reconstruction as well. Specifically, if the interface energy $\Delta \sigma'$ for WZ nuclei (stacking fault energy) is reduced or even becomes negative, PD and "metastable" crystal phase formation would be possible. Density functional theory calculation indeed reveals that the stacking fault energy is surface reconstruction dependent on GaAs (111) *B* [73]. Accordingly, it has already been demonstrated that twinning GaAsSb or GaAs layers forms under GaAs (111) *B* (2×2) reconstruction while the twin formation is suppressed when the surface is $(\sqrt{19} \times \sqrt{19})$ reconstructed [74–76]. Higher twin density is also observed in GaAs NW SAE at lower growth temperature, which is attributed to the (2×2) surface formation [48,51]. Therefore, as the first step to understanding the polytypic InAs NW SAE, the growth front InAs (111) *B* surface needs to be analyzed.

B. Reconstruction of the InAs (111) *B* surface

The InAs (111) *B* surface presents two stable surface reconstructions: the (1×1) and (2×2). It adopts (2×2) reconstruction under the As-rich condition, while the (1×1) shows up in inverse conditions (In rich) [77]. As shown in Fig. 2, the (2×2) surface has additional arsenic trimers on top, while the (1×1) surface is nominally unreconstructed [78–82]. The transition between (1×1) and (2×2) reconstructions is linked with the formation and desorption of arsenic trimers.

We used RHEED to characterize the transition between surface reconstructions. InAs (111) *B* substrate was introduced in the III–V chamber of a Riber MBE system, where the temperature was controlled by a thermocouple and calibrated with optical pyrometer. The sample was first deoxidized at 630 °C with As$_4$ pressure of 1×10^{-5} Torr until the surface shows a clear (1×1) reconstruction [Fig. 3(a)]. The temperature was then gradually decreased while As$_4$ pressure was kept as 1×10^{-5} Torr until the (2×2) reconstruction RHEED pattern was clearly observed [Fig. 3(b)]. The corresponding transition temperature was recorded. The same procedure was then performed for varied As$_4$ pressures from 1×10^{-5} to 4×10^{-6} Torr. It should be noticed that the transition between these two reconstructions is reversible and there is a transition state in between. The logarithm of As$_4$ pressure is plotted
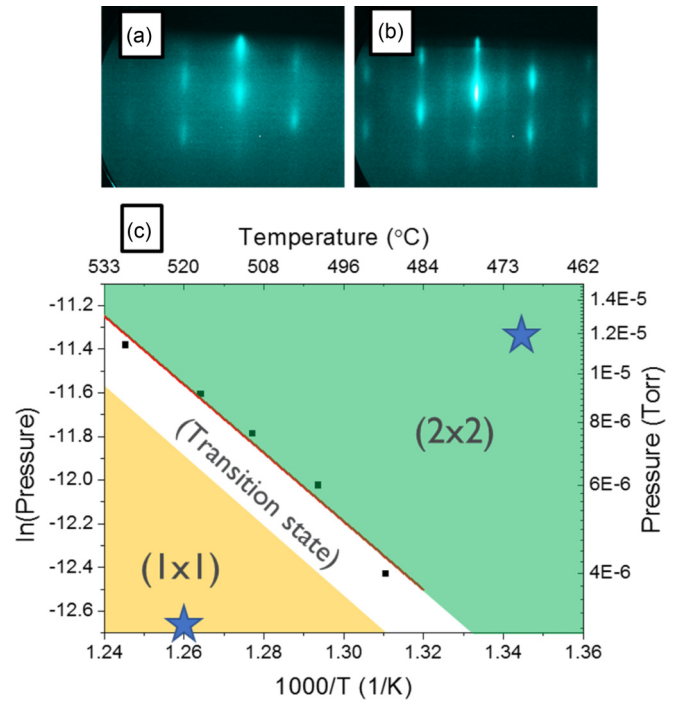

FIG. 3. (a),(b) RHEED patterns of (1×1) and (2×2) surface reconstruction on InAs (111)*B* substrate, respectively. (c) InAs (111)*B* surface reconstruction phase diagram. The As$_4$ beam equivalent pressure is plotted in log scale vs the reciprocal of temperature. The phase boundary is determined by the clear appearance of (2×2) reconstruction. A linear fitting is done on the phase boundary with an activation energy 1.29 eV extracted. It should be noticed that there is a transition state between the two states, which is plotted schematically. The typical (1×1) and (2×2) conditions used for InAs homoepitaxy are marked by stars in the picture as well.

as a function of the reciprocal of transition temperature in Fig. 3(c), which constructs the phase diagram of these two surface reconstructions. As expected, a (2×2) surface shows up under low temperature and high As$_4$ pressure As-rich conditions. In this Arrhenius plot, the activation energy of the transition can be obtained around 1.29 eV by linear fitting of the data points [red line in Fig. 3(c)]. Its physical meaning will be discussed later.

C. Homoepitaxy on InAs (111) *B*

The impact of surface reconstruction on nucleation is then analyzed. For this purpose, InAs homoepitaxy on (111)*B* surface is performed under typical (1×1) and (2×2) conditions. For (1×1) condition, As$_4$ overpressure was 3×10^{-6} Torr and temperature was 520 °C, while (2×2) was 1.2×10^{-5} Torr and 470 °C. The conditions are marked in the phase diagram in Fig. 3(c). The nominal growth rate was kept the same at 0.026 nm/s and growth time was 20 min. AFM was then conducted on these two samples, and their 10 μm $\times$ 10 μm microscopy pictures are shown in Figs. 4(a) and 4(b), respectively. Both samples show rough surface and evidence of island coalescence. In the sample grown under (1×1) type conditions, the surface is full of islands with irregular shape. In
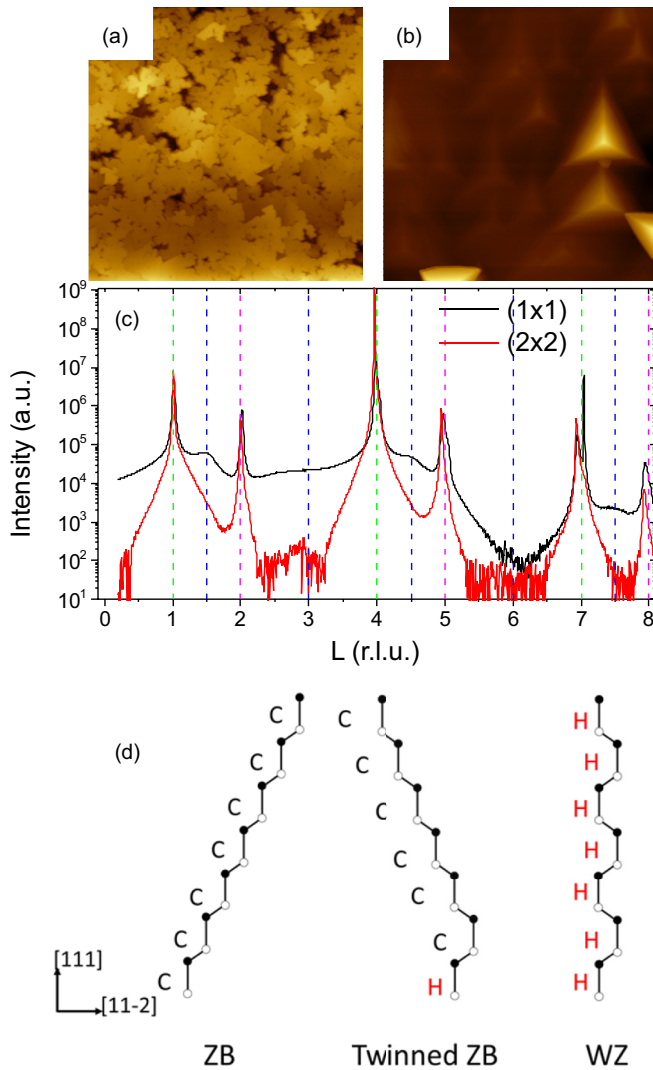
FIG. 4. AFM morphology pictures of InAs (111)*B* homoepitaxy under typical condition of (a) (1 × 1) and (b) (2 × 2) surface reconstructions, respectively. (c) InAs (1 0 *L*) CTRs of these two samples, plotted in black and red respectively. The green, purple, and blue dashed lines indicate the characteristic peaks for pure ZB, twinned ZB, and pure WZ phase diffractions respectively. (d) Schematic plot of atomic chains of ZB, twinned ZB, and WZ structures in [111]/[0001] direction. The cubic and hexagonal layers (PDs) are denoted as C or H, respectively.

contrast, the (2 × 2)-type growth results in merged pyramids, consisting of atomic steps.

To analyze the crystal structure of the homoepitaxial layer, synchrotron GIXRD was conducted on these samples with a grazing angle of 0.3°. It is known that WZ and ZB phase crystals have different diffraction patterns due to their distinctive structure factors [83–85]. For convenience, a set of hexagonal coordinates based on a hexagonal unit cell defined by $a = [1/2, 0, -1/2]_{cubic}$, $b = [0, -1/2, -1/2]_{cubic}$, and $c = [-1, -1, -1]_{cubic}$ are used here. The measured InAs (1 0 *L*) crystal truncation rods (CTRs) of (1 × 1) and (2 × 2) samples are shown in black and red, respectively, in Fig. 4(c), where background intensities have been subtracted. The diffraction peak positions corresponding to the ZB phase ($L = 1, 4$, and

7), the twinned ZB ($L = 2, 5$, and 8), and the WZ phase ($L = 1.5, 3, 4.5, 6$, and 7.5) are indicated by green, red, and blue dashed lines, respectively. Their crystal structures are schematically plotted in Fig. 4(d). It should be noticed that the twinned ZB here denotes the crystal structure that mirrors or has 180° plane rotation regarding to the reference ZB structure. It is caused by the introduction of an odd number of PD(s) underneath and still can be viewed as ZB structure.

Both samples show strong ZB diffraction peaks, which is mainly from the InAs substrate. The most significant difference between these two scans is the unique presence of WZ diffraction in the (1 × 1) sample. Nevertheless, this series of WZ peaks have different intensities. It is known that the integral intensity of a specific diffraction is a function of structure factor, polarization factor, absorption factor, texture factor, and multiplicities [86]. A rough estimation of the WZ diffraction intensities is conducted based on structure factors and corresponding polarization factors [87]. The calculated intensity of (1 0 1.5), (1 0 3), (1 0 4.5), (1 0 6), and (1 0 7.5) diffraction is 99.1%, 40.3%, 89.7%, 1.6%, and 22.8% of the maximum intensity of diffraction, respectively. The trend of the observed intensities agrees well with the calculated ones. Therefore, the formation of WZ InAs in homoepitaxy under typical (1 × 1) reconstruction is confirmed.

Apart from ZB and WZ diffractions, both samples also exhibit considerable twinned ZB diffractions. Nevertheless, it does not correlate to the number of twins in the epilayer, because a single twin is sufficient to rotate the following crystal segment by 180°, which will all contribute to the twinned ZB diffraction. Besides, there are some differences in the tail of the peaks between these two samples. It is attributed to diffuse scattering, which is further related to the surface roughness [88,89].

This polytypic growth in InAs homoepitaxy is related to the nucleation step. PD nucleation has already been reported for various III–V blanket growths on the {111}/{0001} surface by MBE. Except for the twinning GaAs formation shown in Sec. IV A, the ZB phase GaN forms under low growth temperature and high V/III ratio. STM experiment confirms it is related to PD nucleation [90]. In addition, PD nucleation is also observed on InAs (111)*B* homoepitaxy, although in a recrystallization manner. After high-temperature annealing under an As atmosphere, widely spread twin islands were observed by scanning tunneling microscope [81]. Here we further confirm that on the InAs (111)*B* surface, the crystalline preference in nucleation is surface reconstruction dependent. WZ phase crystal is formed under (1 × 1) reconstruction conditions while basically ZB under (2 × 2). As we will show in the following sections, that is the starting point to understanding the polytypism in InAs NW SAE.

V. IMPACT OF SURFACE RECONSTRUCTION ON NW POLYTYPISM

In Sec. III, the dependence of NW hexagonality on growth parameters is presented. Among all the parameters, temperature and group-V partial pressure are critical in InAs NW polytypism control. Coincidently, these two parameters also govern the surface reconstruction of InAs (111)*B*. As we have seen in Sec. IV, the surface reconstruction indeed has a
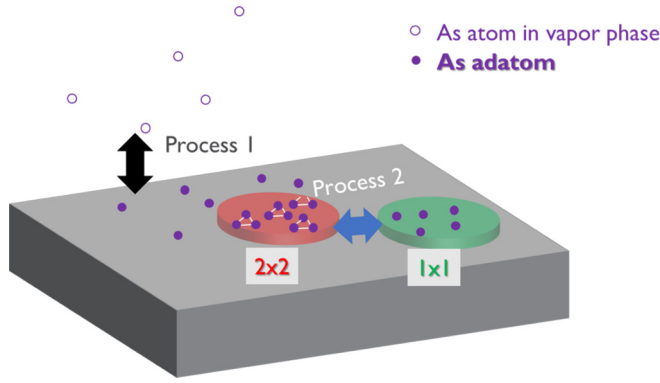
FIG. 5. Schematic illustration of the surface reconstruction model on InAs (111)*B*. Two processes are involved: (1) the adsorption of As adatoms on (111)*B* surface, and (2) the reversible inter-change of (1 × 1) and (2 × 2) reconstructions. As atoms in vapor phase are represented by empty purple dots, and the adatoms by solid ones. We assume the nuclei are either (1 × 1) or (2 × 2) reconstructed. The nucleus with (1 × 1) reconstruction on top is plotted in green while the (2 × 2) is in red. It should be noticed that the As atoms plotted on (2 × 2) surface are in the form of As trimer which is chemically bonded to the top (111)*B* layer. An event of breaking the bond in As trimer on (2 × 2) surface and releasing an As adatom is illustrated as well.

significant influence on crystal structure in the homoepitaxial InAs layer on the (111)*B* surface. Hence, it is worth analyzing how surface reconstruction contributes to polytypism phenomenon in NW SAE.

However, in NW SAE, the direct characterization of surface reconstruction is difficult. In this section, we build a model that links growth conditions to the surface reconstruction of nuclei. This reveals the relation between polytypism in InAs NW and the surface reconstruction of the growth front.

A. Surface reconstruction transition model

We first model the transition of surface reconstruction on nuclei by an absorption model. As depicted in Fig. 5, the first process that needs to be taken into account is the physical adsorption of As adatoms (solid dots). It is a reversible reaction with As atoms in the vapor phase (empty dots) which is termed as process 1 in Fig. 5. We consider a Langmuir kinetics for this adsorption process. The area concentration (i.e., fractional occupancy of the adsorption sites) of As adatoms C_{As} is related to the As partial pressure P_{As} by the equation

$$C_{As} = \frac{b P_{As}}{1 + b P_{As}}; \tag{5}$$

b is the equilibrium constant, which is related to the Gibbs free energy of the physical adsorption. In the case studied here, the As partial pressure can be replaced by TBAs or As_4 flow rate f_{As} since the steady state is reached in the reactor chamber. Therefore, Eq. (5) can be rewritten as

$$C_{As} = \frac{b f_{As}}{1 + b f_{As}}. \tag{6}$$

With a determined As adatom concentration on the surface, the second process to be examined is the transition between (1 × 1) and (2 × 2) surface reconstruction itself (process 2 in

Fig. 5). Here we assume that the top of the nuclei is either (1 × 1) or (2 × 2) reconstructed, that is, the possibility of intermixing of these two reconstructions on a single nucleus is excluded. Structurally, the difference of these two reconstructions is the additional As trimer on the (2 × 2) surface, which is chemically bonded to the (111)*B* surface [Fig. 2(b)]. The formation of (2 × 2) reconstruction is related to the chemical adsorption of As adatoms, a scenario similar to what happens on the (2 × 2) reconstructed GaAs (111)*B* surface [91,92]. The aforementioned transition of surface reconstruction can be viewed as a reversible reaction with As adatoms involved: As adatom + (1 × 1) ⇌ (2 × 2). If we assume that the reaction follows a first-order rate equation, in equilibrium, the reaction can be depicted as

$$k_f C_{As} C_{(1 \times 1)} = k_r C_{(2 \times 2)}, \tag{7}$$

where C_{As}, $C_{(1\times1)}$, and $C_{(2\times2)}$ are the concentration of As adatoms, (1 × 1) reconstruction area, and (2 × 2) area, respectively. k_f and k_r are the forward and reverse rate constants, respectively. The ratio $\frac{k_f}{k_r}$ has an exponential term, that is, $\frac{k_f}{k_r} \propto \exp(E_A/kT)$, where E_A is the activation energy. As adatom concentration has been already obtained in Eq. (6). Therefore, combining Eqs. (6) and (7), the ratio between (1 × 1) and (2 × 2) reconstructions is

$$\frac{C_{(2 \times 2)}}{C_{(1 \times 1)}} \propto \frac{\exp(E_A/kT) \, b f_{As}}{1 + b f_{As}}. \tag{8}$$

This model can explain the experimental result of surface reconstruction shown in Fig. 3. In that experiment, the boundary between (1 × 1) and (2 × 2) reconstruction is plotted based on the appearance of characteristic (2 × 2) reconstructed RHEED pattern. The boundary line in principle corresponds to a (2 × 2) dominant surface. Without loss of generality, the ratio of $\frac{C_{(2 \times 2)}}{C_{(1 \times 1)}}$ is set as a certain constant value for the boundary. In other words, at the boundary we have

$$\frac{C_{(2 \times 2)}}{C_{(1 \times 1)}} \propto \frac{\exp\left(\frac{E_A}{kT}\right) b f_{As}}{1 + b f_{As}} = \text{const.} \tag{9}$$

Because the adatom density C_{As} is normally very low [93–95], as demonstrated in Eq. (5), it is reasonable to assume $b f_{As} \ll 1$. Hence, the relationship between temperature and As pressure at the boundary can be deduced from Eq. (9) as

$$\ln P_{As} = A - \frac{E_A}{k} \frac{1}{T}, \tag{10}$$

where A is an arbitrary constant. This equation describes the linear relationship between $\frac{1}{T}$ and $\ln P_{As}$, as demonstrated in Fig. 3. The activation energy derived from the slope is actually E_A, the activation energy involved in process 2.

B. Relationship between hexagonality and surface reconstruction

In Eq. (8) we got the probabilities of nuclei with the two surface reconstructions as a function of temperature and TBAs flow rate. The next step is to link this to the hexagonality in InAs NWs. Based on the discussion in Sec. IV, we can make an assumption that the (1 × 1) reconstructed InAs nucleus on the (111)*B* surface tends to be in WZ phase while the
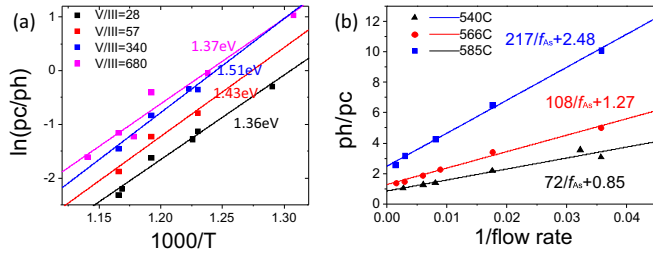
FIG. 6. (a) The natural logarithm of cubic to hexagonal phase ratio p_c/p_h is plotted as a function of reciprocal of growth temperature under four sets of V/III ratios. Linear fitting is done on each data set and corresponding activation energies are shown with the corresponding color as well. (b) The ratio of p_h/p_c vs the reciprocal of TBAs flow rate under three sets of growth temperatures. Linear fitting is conducted on each data set with corresponding fitted parameters shown respectively.

(2×2) reconstructed one will take the ZB phase. The NW hexagonality is equal to the probability of PD nucleation due to the layer-by-layer growth (i.e., the mononucleation event for each layer). In this way, the hexagonality of the NW is finally correlated to the probability of forming (1×1)-type and (2×2)-type nuclei. The ratio between the ZB to WZ phases can be deduced as

$$\frac{p_c}{p_h} = \frac{C_{(2 \times 2)}}{C_{(1 \times 1)}} \propto \frac{\exp(E_A/kT)\, b f_{As}}{1 + b f_{As}}, \qquad (11)$$

where p_c and p_h are the frequency of ZB (cubic) and WZ (hexagonal) segments in InAs NWs, respectively. It is a quantitative relationship between hexagonality of InAs NWs and growth conditions. We are able to verify the model by the input of hexagonality values extracted from XRD results [57].

First, the temperature effect is studied on InAs NWs grown under varied V/III ratios ranging from 28 to 680. For this purpose, Eq. (11) can be rewritten as

$$\ln\left(\frac{p_c}{p_h}\right) \propto \ln\left(\frac{b f_{As}}{1 + b f_{As}}\right) + \frac{E_A}{kT}. \qquad (12)$$

For each V/III ratio, a series of growth temperatures were applied ranging from 490 to 605 °C within the NW growth window. The TMIn flow rate was kept at 1 μmol/min. The ratio p_c/p_h in Eq. (12) can be obtained by $\frac{1-\text{hex}}{\text{hex}}$, where hex is the hexagonality value obtained from InAs mixed-phase peak position in XRD. For each V/III ratio, the logarithm of ratio p_c/p_h is plotted against the reciprocal of growth temperature in Fig. 6(a). The activation energy values extracted from these Arrhenius plots are shown in corresponding colors as well. The activation energy obtained here is E_A. Surprisingly, irrespective of the huge difference in TBAs flow rate, the slopes of all Arrhenius plots are nearly the same, indicating similar E_A values ranging from 1.36 to 1.51 eV. Since E_A is directly linked to the rate constant, this echoes the common knowledge that the reaction rate constant is independent of reactant concentration (i.e., TBAs flow rate). Besides, this E_A value extracted from the hexagonality experiment is very close to that obtained by the surface reconstruction experiment (1.29 eV), which further supports our model.

Next, this model is further validated in the analysis of the V/III ratio. To this end, Eq. (11) is rewritten as

$$\frac{p_h}{p_c} \propto \frac{\exp\left(-\frac{E_A}{kT}\right)}{b} \frac{1}{f_{As}} + \exp\left(-\frac{E_A}{kT}\right). \qquad (13)$$

InAs NWs were grown under varied V/III ratios under three sets of temperatures [some of the data are shared with the temperature study shown in Fig. 6(a)]. The ratio of p_h/p_c is plotted as a function of reciprocal TBAs flow rate $1/f_{As}$ in Fig. 6(b). Linear trends are observed irrespective of growth temperature, which agrees with Eq. (13). The fitted equations are also listed in the figure as well. It is interesting to notice that the ratios between intercept and slope are nearly constant around 0.012. This indicates that the parameter b is less temperature sensitive. It could be due to that process 1 is physical adsorption [96], and the energy term involved in b is much smaller than that in process 2, which is chemical adsorption with the formation of chemical bonds [97].

The quantitative agreement between experimental data and the model strongly suggests that the polytypism in InAs NWs is related to the reconstruction on InAs (111)B surface, or strictly speaking, to the reconstruction of the top surface of nuclei. In fact, the (1×1) surface is not literally unreconstructed. Instead, both surface In and As atoms are relaxed perpendicularly to the surface and the dangling electrons from As anions on surface are transferred to the second layer In cations [78,98]. In contrast, on the (2×2) surface, while there are several components of relaxed surface As atoms, the surface In atoms have little relaxation [80]. In consequence, one possible explanation is that the stacking fault energy in (1×1) reconstructed nuclei could be changed and even turned to negative by strain [99,100], and WZ phase crystal structure becomes more favorable.

VI. CONCLUSIONS

In this work, the correlation between polytypism in InAs SAE NWs and surface reconstruction of NW growth front $(111)B$ is identified. Followed by the study of the dependence of the $(111)B$ surface reconstruction on temperature and As partial pressure, we first reveal that polytypism is related to surface reconstruction in homoepitaxy on InAs (111)B substrate. For InAs NW SAE, a model is built to link hexagonality to growth conditions quantitatively, based on the assumption that surface reconstruction governs the stable crystal structure of nuclei. The good agreement between our model and experimental data strongly support this hypothesis and evidences this correlation.

Practically, the impact of various growth parameters on polytypism is extensively studied in InAs NW SAE. It provides a guide for crystal phase control. Based on this study, we manage to control the crystal structure of InAs NW by SAE. The WZ phase InAs NW with hexagonality of 93% is finally achieved.

[1] L. Wernersson, C. Thelander, E. Lind, and L. Samuelson, Proc. IEEE **98**, 2047 (2010).

[2] S. Li and A. Waag, J. Appl. Phys. **111**, 71101 (2012).

[3] R. S. Wagner and W. C. Ellis, Appl. Phys. Lett. **4**, 89 (1964).

[4] E. Givargizov, J. Cryst. Growth **31**, 20 (1975).

[5] K. Hiruma and M. Yazawa, J. Appl. Phys. **74**, 3162 (1993).

[6] K. Hiruma and M. Yazawa, J. Appl. Phys. **77**, 447 (1995).

[7] W. Seifert, M. Borgström, K. Deppert, K. A. Dick, J. Johansson, M. W. Larsson, T. Mårtensson, N. Sköld, C. Patrik, T. Svensson, B. A. Wacaser, L. Reine Wallenberg, and L. Samuelson, J. Cryst. Growth **272**, 211 (2004).

[8] X. Duan and C. M. Lieber, Adv. Mater. **12**, 298 (2000).

[9] J. Motohisa, J. Noborisaka, J. Takeda, M. Inari, and T. Fukui, J. Cryst. Growth **272**, 180 (2004).

[10] K. Tomioka, M. Yoshimura, and T. Fukui, Nature (London) **488**, 189 (2012).

[11] K. Takahashi and T. Morizumi, Jpn. J. Appl. Phys. **5**, 657 (1966).

[12] M. Koguchi, H. Kakibayashi, M. Yazawa, K. Hiruma, and T. Katsuyama, Jpn. J. Appl. Phys **31**, 2061 (1992).

[13] J. Johansson, L. S. Karlsson, C. P. T. Svensson, T. Mårtensson, B. A. Wacaser, K. Deppert, L. Samuelson, and W. Seifert, Nat. Mater. **5**, 574 (2006).

[14] F. Glas, J.-C. Harmand, and G. Patriarche, Phys. Rev. Lett. **99**, 146101 (2007).

[15] M. Moewe, L. C. Chuang, V. G. Dubrovskii, and C. Chang-Hasnain, J. Appl. Phys. **104**, 44313 (2008).

[16] H. Shtrikman, R. Popovitz-Biro, A. Kretinin, and M. Heiblum, Nano Lett. **9**, 215 (2009).

[17] H. Shtrikman, R. Popovitz-Biro, A. Kretinin, L. Houben, M. Heiblum, M. Bukała, M. Galicka, R. Buczko, and P. Kacman, Nano Lett. **9**, 1506 (2009).

[18] R. E. Algra, M. A. Verheijen, M. T. Borgström, L.-F. Feiner, G. Immink, W. J. P. van Enckevort, E. Vlieg, and E. P. A. M. Bakkers, Nature (London) **456**, 369 (2008).

[19] K. A. Dick, C. Thelander, L. Samuelson, and P. Caroff, Nano Lett. **10**, 3494 (2010).

[20] H. J. Joyce, J. Wong-Leung, Q. Gao, H. H. Tan, and C. Jagadish, Nano Lett. **10**, 908 (2010).

[21] P. Krogstrup, R. Popovitz-Biro, E. Johnson, M. H. Madsen, J. Nygård, and H. Shtrikman, Nano Lett. **10**, 4475 (2010).

[22] P. Caroff, J. Bolinsson, and J. Johansson, IEEE J. Sel. Top. Quantum Electron. **17**, 829 (2011).

[23] D. Jacobsson, F. Panciera, J. Tersoff, M. C. Reuter, S. Lehmann, S. Hofmann, K. A. Dick, and F. M. Ross, Nature (London) **531**, 317 (2016).

[24] K. Tomioka, J. Motohisa, S. Hara, and T. Fukui, Jpn. J. Appl. Phys. **46**, L1102 (2007).

[25] K. Ikejiri, Y. Kitauchi, K. Tomioka, J. Motohisa, and T. Fukui, Nano Lett. **11**, 4314 (2011).

[26] M. D. Schroer and J. R. Petta, Nano Lett. **10**, 1618 (2010).

[27] C. Thelander, P. Caroff, S. Plissard, A. W. Dey, and K. A. Dick, Nano Lett. **11**, 2424 (2011).

[28] Q. Gao, D. Saxena, F. Wang, L. Fu, S. Mokkapati, Y. Guo, L. Li, J. Wong-Leung, P. Caroff, H. H. Tan, and C. Jagadish, Nano Lett. **14**, 5206 (2014).

[29] G. Bussone, H. Schäfer-Eberwein, E. Dimakis, A. Biermanns, D. Carbone, A. Tahraoui, L. Geelhaar, P. Haring Bolívar, T. U. Schülli, and U. Pietsch, Nano Lett. **15**, 981 (2015).

[30] N. Vainorius, S. Lehmann, D. Jacobsson, L. Samuelson, K. A. Dick, and M.-E. Pistol, Nano Lett. **15**, 2652 (2015).

[31] S. Assali, I. Zardo, S. Plissard, D. Kriegner, M. A. Verheijen, G. Bauer, A. Meijerink, A. Belabbes, F. Bechstedt, J. E. M. Haverkort, and E. P. A. M. Bakkers, Nano Lett. **13**, 1559 (2013).

[32] G. C. Trigunayat, Solid State Ionics **48**, 3 (1991).

[33] Y. M. Tairov and V. F. Tsvetkov, Prog. Cryst. Growth Charact. **7**, 111 (1983).

[34] S. Paiman, Q. Gao, H. H. Tan, C. Jagadish, K. Pemasiri, M. Montazeri, H. E. Jackson, L. M. Smith, J. M. Yarrison-Rice, X. Zhang, and J. Zou, Nanotechnology **20**, 225606 (2009).

[35] J. Johansson, K. A. Dick, P. Caroff, M. E. Messing, J. Bolinsson, K. Deppert, and L. Samuelson, J. Phys. Chem. C **114**, 3837 (2010).

[36] S. Lehmann, J. Wallentin, D. Jacobsson, K. Deppert, and K. A. Dick, Nano Lett. **13**, 4099 (2013).

[37] E. Husanu, D. Ercolani, M. Gemmi, and L. Sorba, Nanotechnology **25**, 205601 (2014).

[38] J. Arbiol, S. Estradé, J. D. Prades, A. Cirera, F. Furtmayr, C. Stark, A. Laufer, M. Stutzmann, M. Eickhoff, M. H. Gass, A. L. Bleloch, F. Peiró, and J. R. Morante, Nanotechnology **20**, 145704 (2009).

[39] B. Mandl, K. A. Dick, D. Kriegner, M. Keplinger, G. Bauer, J. Stangl, and K. Deppert, Nanotechnology **22**, 145603 (2011).

[40] M. Pozuelo, S. V. Prikhodko, R. Grantab, H. Zhou, L. Gao, S. D. Sitzman, V. Gambin, V. B. Shenoy, R. F. Hicks, and S. Kodambaka, J. Cryst. Growth **312**, 2305 (2010).

[41] P. Caroff, K. Dick, J. Johansson, M. E. Messing, K. Deppert, and L. Samuelson, Nat. Nanotechnol. **4**, 50 (2009).

[42] K. A. Dick, J. Bolinsson, M. E. Messing, S. Lehmann, J. Johansson, and P. Caroff, J. Vac. Sci. Technol., B: Microelectron. Nanometer Struct.–Process., Meas., Phenom. **29**, 04D103 (2011).

[43] C. Y. Yeh, Z. W. Lu, S. Froyen, and A. Zunger, Phys. Rev. B **46**, 10086 (1992).

[44] T. Akiyama, K. Sano, K. Nakamura, and T. Ito, Jpn. J. Appl. Phys. **45**, L275 (2006).

[45] V. G. Dubrovskii and N. V. Sibirev, Phys. Rev. B **77**, 035414 (2008).

[46] F. Ishizaka, Y. Hiraya, K. Tomioka, and T. Fukui, J. Cryst. Growth **411**, 71 (2015).

[47] Y. Kitauchi, Y. Kobayashi, K. Tomioka, S. Hara, K. Hiruma, T. Fukui, and J. Motohisa, Nano Lett. **10**, 1699 (2010).

[48] H. Yoshida, K. Ikejiri, T. Sato, S. Hara, K. Hiruma, J. Motohisa, and T. Fukui, J. Cryst. Growth **312**, 52 (2009).

[49] Y. Kohashi, T. Sato, K. Ikejiri, K. Tomioka, S. Hara, and J. Motohisa, J. Cryst. Growth **338**, 47 (2012).

[50] M. Yao, C. Sheng, M. Ge, C. Y. Chi, S. Cong, A. Nakano, P. D. Dapkus, and C. Zhou, ACS Nano **10**, 2424 (2016).

[51] J. N. Shapiro, A. Lin, C. Ratsch, and D. L. Huffaker, Nanotechnology **24**, 475601 (2013).

[52] K. Ikejiri, J. Noborisaka, S. Hara, J. Motohisa, and T. Fukui, J. Cryst. Growth **298**, 616 (2007).

[53] D. Rudolph, S. Hertenberger, S. Bolte, W. Paosangthong, D. Spirkoska, M. Döblinger, M. Bichler, J. J. Finley, G. Abstreiter, and G. Koblmüller, Nano Lett. **11**, 3848 (2011).

[54] M. Björk, H. Schmid, and C. Breslin, J. Cryst. Growth **344**, 31 (2012).

[55] C.-Y. Chi, C.-C. Chang, S. Hu, T.-W. Yeh, S. B. Cronin, and P. D. Dapkus, Nano Lett. **13**, 2506 (2013).

[56] A. C. Farrell, W.-J. Lee, P. Senanayake, M. A. Haddad, S. V. Prikhodko, and D. L. Huffaker, Nano Lett. **15**, 6614 (2015).

[57] Z. Liu, C. Merckling, M. Caymax, R. Rooyackers, N. Collaert, A. Thean, O. Richard, H. Bender, W. Vandervorst, and M. Heyns, Cryst. Growth Des. **15**, 3868 (2015).

[58] J. Rubio-Zuazo, P. Ferrer, A. Lopez, A. Gutierrez-Leon, I. Da Silva, and G. R. Castro, Nucl. Instrum. Methods Phys. Res. Sect. A **716**, 23 (2013).

[59] V. G. Dubrovskii, N. V. Sibirev, J. C. Harmand, and F. Glas, Phys. Rev. B **78**, 235301 (2008).

[60] B. O. Jung, S.-Y. Bae, Y. Kato, M. Imura, D.-S. Lee, Y. Honda, and H. Amano, CrystEngComm **16**, 2273 (2014).

[61] S. D. Hersee, X. Sun, and X. Wang, Nano Lett. **6**, 1808 (2006).

[62] Z. Zhang, Y. Wang, H. Li, W. Yuan, X. Zhang, C. Sun, and Z. Zhang, ACS Nano **10**, 763 (2016).

[63] I. Soshnikov, G. Cirlin, A. Tonkikh, Y. B. Samsonenko, V. Dubovskii, V. Ustinov, O. Gorbenko, D. Litvinov, and D. Gerthsen, Phys. Solid State **47**, 2213 (2005).

[64] J. Arbiol, A. Fontcuberta i Morral, S. Estradé, F. Peiró, B. Kalache, P. Roca i Cabarrocas, and J. R. Morante, J. Appl. Phys. **104**, 64312 (2008).

[65] I. V. Markov, *Crystal Growth for Beginners: Fundamentals of Nucleation, Crystal Growth and Epitaxy*, 2nd ed. (World Scientific, Singapore, 2003).

[66] F. Glas, G. Patriarche, and J. C. Harmand, J. Phys.: Conf. Ser. **209**, 12002 (2010).

[67] J. Johansson, L. S. Karlsson, K. A. Dick, J. Bolinsson, B. A. Wacaser, K. Deppert, and L. Samuelson, Cryst. Growth Des. **9**, 766 (2009).

[68] T. Chiaramonte, L. H. G. Tizei, D. Ugarte, and M. A. Cotta, Nano Lett. **11**, 1934 (2011).

[69] X. Yu, H. Wang, J. Lu, J. Zhao, J. Misuraca, P. Xiong, and S. von Molnár, Nano Lett. **12**, 5436 (2012).

[70] J. Johansson, J. Bolinsson, M. Ek, P. Caroff, and K. A. Dick, ACS Nano **6**, 6142 (2012).

[71] J. Johansson, Z. Zanolli, and K. A. Dick, Cryst. Growth Des. **16**, 371 (2016).

[72] C. B. Duke, Chem. Rev. **96**, 1237 (1996).

[73] H. Koga, Phys. Rev. B **82**, 113301 (2010).

[74] S. Naritsuka, S. Matsuoka, T. Kondo, K. Saitoh, T. Suzuki, Y. Yamamoto, and T. Maruyama, J. Cryst. Growth **301-302**, 42 (2007).

[75] Y. R. Chen, L. C. Chou, Y. J. Yang, and H. H. Lin, J. Phys. D: Appl. Phys. **46**, 35306 (2013).

[76] T. Hayakawa, M. Morishima, and S. Chen, Appl. Phys. Lett. **59**, 3321 (1991).

[77] A. Ohtake and K. Mitsuishi, J. Vac. Sci. Technol., B: Microelectron. Nanometer Struct.–Process., Meas., Phenom. **29**, 31804 (2011).

[78] C. Andersson, L. Olsson, L. Ilver, U. Karlsson, J. Kanski, C. Andersson, L. Olsson, L. Ilver, and U. Karlsson, J. Phys. IV **4**, 209 (1994).

[79] C. B. M. Andersson, U. O. Karlsson, M. C. Hakansson, L. Ö. Olsson, L. Ilver, J. Kanski, P.-O. Nilsson, and P. E. S. Persson, Surf. Sci. **307-309**, 885 (1994).

[80] C. B. M. Andersson, U. O. Karlsson, M. C. Håkansson, L. Ö. Olsson, L. Ilver, J. Kanski, and P.-O. Nilsson, Surf. Sci. **347**, 199 (1996).

[81] E. Hilner, E. Lundgren, and A. Mikkelsen, Surf. Sci. **604**, 354 (2010).

[82] A. Taguchi, J. Cryst. Growth **278**, 468 (2005).

[83] J. Eymery, F. Rieutord, V. Favre-Nicolin, O. Robach, Y. M. Niquet, L. Fröberg, T. Mårtensson, and L. Samuelson, Nano Lett. **7**, 2596 (2007).

[84] A. Davydok, Ph.D. thesis, Univeristy of Siegen, 2013.

[85] M. Takahasi, M. Kozu, T. Sasaki, and W. Hu, Cryst. Growth Des. **15**, 4979 (2015).

[86] M. Birkholz, *Thin Film Analysis by X-Ray Scattering* (Wiley-VCH Verlag, Weinheim, 2006).

[87] D. C. Palmer, Z. Kristallogr. **230**, 559 (2015).

[88] S. R. Andrews and R. A. Cowley, J. Phys. C: Solid State Phys. **18**, 6427 (1985).

[89] G. Renaud, Surf. Sci. Rep. **32**, 5 (1998).

[90] B. M. Shi, M. H. Xie, H. S. Wu, N. Wang, and S. Y. Tong, Appl. Phys. Lett. **89**, 151921 (2006).

[91] K. Yang and L. J. Schowalter, Appl. Phys. Lett. **60**, 1851 (1992).

[92] T. Nishida, K. Uwai, Y. Kobayashi, and N. Kobayashi, Jpn. J. Appl. Phys. **34**, 6326 (1995).

[93] Z. W. Wang and R. E. Palmer, Nano Lett. **12**, 91 (2012).

[94] E. Wahlstrom, I. Ekvall, H. Olin, and L. Wallden, Appl. Phys. A **66**, 1107 (1998).

[95] J. A. Nieminen and K. Kaski, Phys. Rev. A **40**, 2088 (1989).

[96] T. Watanabe, A. Ichikawa, M. Sakuraba, T. Matsuura, and J. Murota, J. Electrochem. Soc. **145**, 4252 (1998).

[97] D. McQuarrie and J. Simon, *Physical Chemistry, A Molecular Approach* (University Science Books, Sausalito, CA, 1997).

[98] S. Mankefors, P. O. Nilsson, and J. Kanski, Surf. Sci. **443**, L1049 (1999).

[99] H. Hibino and T. Ogino, Mater. Sci. Eng., B **87**, 214 (2001).

[100] A. Fissel, E. Bugiel, C. R. Wang, and H. J. Osten, J. Cryst. Growth **290**, 392 (2006).